Mapping Interior Strain Fields in Thick Composites and Sandwich Plates With Digital Volumetric Speckle Photography Technique

Lingtao Mao and Fu-Pen Chiang

1 Introduction

Optical full-field measurement techniques such as speckle photography [1], speckle interferometry [2], geometric moire [3], moire interferometry [4], digital speckle photography (DSP) [5] and digital image correlation (DIC) [6, 7] have all been applied to determining properties of composite materials [8]. Thanks to their simplicity, DSP and DIC have become ubiquitous in recent years as the preferred tools. However, all these full–field measurements techniques can only measure surface displacement of the specimen. Due to material heterogeneity at different length scales, the deformation of a composite structure is always 3D in nature. Thus, a 2D surface measurement technique can never fully reveal the failure mechanism of composites. As a result whenever a naval composite structure is designed, a high safety factor is often used. This adds weight and cost to the resulting structure. Thus there is a strong need to develop a technique whereby one can probe into the interior deformation of solids. While there already exist several stress/strain analysis techniques that can probe the interior of solids (for example frozen-stress photoelasticity [9, 10], moire [11], and embedded speckle method [12, 13]), they all require that the specimen material be transparent, in one case even birefringent.

In recent years X-ray micro-computed tomography (CT) has become a familiar tool in materials research. Applications of micro-CT to composite materials have mainly been concentrated in two fields. One is for the visualization of internal features, such as void measurement, fiber location and waviness, fiber breakage,

L. Mao
State Key Laboratory of Coal Resources and Safe Mining,
China University of Mining & Technology, Beijing, China

F.-P. Chiang (✉)
Laboratory for Experimental Mechanics Research, Department of Mechanical Engineering,
Stony Brook University, Stony Brook, NY, USA
e-mail: fu-pen.chiang@stonybrook.edu

interface delamination, internal damage and crack growth, etc. [14, 15]. The other application deals with internal displacement measurement. Based on the volumetric image capability of CT scanning, Digital Volume Correlation (DVC) technique was proposed to assess the internal displacement fields of solid objects. Roux, et al. [16] used DVC to evaluate the internal displacement of a solid foam. Brault, et al. [17] performed volume kinematic measurements of laminated composite materials with metallic particles imbedded into the specimen for the purpose of contrast enhancement. Lecomte-Grosbras, et al. [18] investigated the free-edge effects in laminate composites by using DVC. Recently we developed an effective 3D experimental strain analysis technique called DVSP (Digital Volumetric Speckle Photography) [19] in which we use the internal features of opaque solids as 3D volumetric speckles. We developed an algorithm to process the CT recorded volumetric speckles in a way similar to the algorithm we developed for the 2D digital speckle photography technique [20, 21]. DVSP can be applied to probing the internal deformation of almost any solid material. We have successfully applied the technique to coal [22], rock [23] and concrete [24]. In this study, we describe in detail the theory and practice of DVSP and its application to composites. Three examples are chosen for the demonstration: a woven composite beam under three-point bending, a woven composite beam with a prepared slot under three-point bending and a foam composite sandwich beam under three-point bending. Displacement and strain distributions of many internal sections were mapped in detail.

2 Theory of Digital Volumetric Speckle Photography (DVSP)

The CT system is used to scan the specimen before and after the application of load. The two reconstructed digital volume images are defined as reference volume image and deformed volume image, respectively. Both digital images are subdivided into volumetric subsets with voxel arrays of 32 voxel $\times$ 32 voxel $\times$ 32 voxel, for example, and 'compared' with the procedures schematically shown in Fig. 1.

Let $h_1(x, y, z)$ and $h_2(x, y, z)$ be gray distribution functions of a pair of generic volumetric speckle subsets, before and after deformation, respectively, and that

$$
\begin{aligned}
h_1(x, y, z) &= h(x, y, z) \\
h_2(x, y, z) &= h[x - u(x, y, z), y - v(x, y, z), z - w(x, y, z)]
\end{aligned}
\tag{1}
$$

where u, v and w components of the displacement vector collectively experienced by the speckles within the subset of voxels along the x, y, and z directions, respectively. A first-step 3D FFT (Fast Fourier Transform) is applied to both h_1 and h_2 yielding
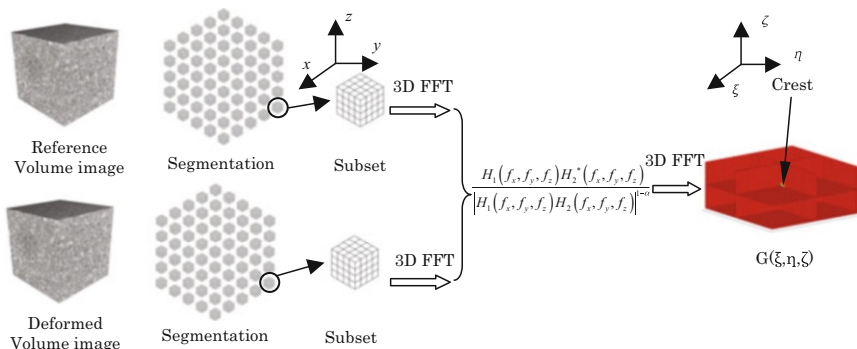
Fig. 1 Schematics demonstrating the processing algorithm of DVSP

$$H_1\left(f_x,f_y,f_z\right) = \Im\{h_1(x,y,z)\} = \left|H\left(f_x,f_y,f_z\right)\right| \exp\left[j\phi\left(f_x,f_y,f_z\right)\right]$$
$$H_2\left(f_x,f_y,f_z\right) = \Im\{h_2(x,y,z)\} = \left|H\left(f_x,f_y,f_z\right)\right| \exp\left\{j\left[\phi\left(f_x,f_y,f_z\right) - 2\pi\left(uf_x + vf_y + wf_z\right)\right]\right\}$$

$$(2)$$

where $H_1(f_x,f_y,f_z)$ is the Fourier transform spectrum of $h_1(x,y,z)$, $H_2(f_x,f_y,f_z)$ is the Fourier transform spectrum of $h_2(x,y,z)$, and $\Im$ stands for Fourier Transform. $|H(f_x,f_y,f_z)|$ and $\phi(f_x,f_y,f_z)$ are the spectral amplitude and phase fields, respectively.

Then, a numerical interference filter between the two 3D speckle patterns is performed at the spectral domain, i.e.

$$F\left(f_x,f_y,f_z\right) = \frac{H_1\left(f_x,f_y,f_z\right)H_2{}^*\left(f_x,f_y,f_z\right)}{\left|H_1\left(f_x,f_y,f_z\right)H_2\left(f_x,f_y,f_z\right)\right|^{1-\alpha}} \qquad (3)$$

in which * stands for the complex conjugate, and α is an appropriate constant $(0 \leq \alpha \leq 1)$.

When $\alpha = 0$, Eq. (3) can be expressed as

$$F\left(f_x,f_y,f_z\right) = H_1\left(f_x,f_y,f_z\right) \frac{\exp\left\{-j\left[\phi\left(f_x,f_y,f_z\right) - 2\pi\left(uf_x + vf_y + wf_z\right)\right]\right\}}{\left|H\left(f_x,f_y,f_z\right)\right|} \quad (4)$$

where $\dfrac{\exp\left\{-j\left[\phi\left(f_x,f_y,f_z\right) - 2\pi\left(uf_x+vf_y+wf_z\right)\right]\right\}}{\left|H\left(f_x,f_y,f_z\right)\right|}$ is essentially an inverse filter (IF).

When $\alpha = 0.5$, Eq. (3) can be expressed as

$$F\left(f_x,f_y,f_z\right) = H_1\left(f_x,f_y,f_z\right) \exp\left\{-j\left[\phi\left(f_x,f_y,f_z\right) - 2\pi\left(uf_x + vf_y + wf_z\right)\right]\right\} \quad (5)$$

where $\exp\{-j[\phi(f_x,f_y,f_z) - 2\pi(uf_x + vf_y + wf_z)]\}$ is a so-called phase-only filter (POF).
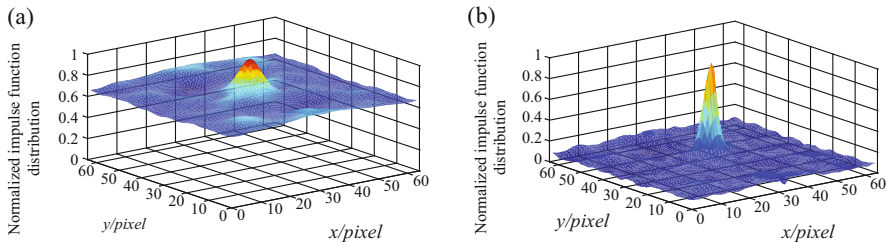
Fig. 2 Normalized impulse function distribution with different filters: (**a**) CMF filter; (**b**) POF filter

When $\alpha = 1$, Eq. (3) can be expressed as

$$F\big(f_x, f_y, f_z\big) = H_1\big(f_x, f_y, f_z\big) H_2{}^*\big(f_x, f_y, f_z\big) \tag{6}$$

where $H_2{}^*(f_x, f_y, f_z)$ can be viewed as a classical matched filter (CMF). When a correlation filter is chosen, peak sharpness and noise tolerance are the factors that need to be considered. In the 2D digital speckle photography technique, α is 0.5, and the algorithm is essentially a POF. The influence of CMF, POF and IF filters on the accuracy of 2D speckle photography were analyzed and the results indicate that IF is extremely sensitive to noise, thus cannot be used as a reliable filter. There is no significant difference between CMF and POF filters [25]. But while the POF filter provides somewhat more accurate estimates of the peak position, the reliability of the CMF filter is better. In Fig. 2, normalized impulse function distributions for the two filters are shown. It is noted that the peak impulse with POF is sharper, which can provide a good compromise between peak sharpness and noise tolerance in the correlation theory.

In this paper, $\alpha = 0.5$ is adopted. As a result, Eq. (3) can then be written as

$$
\begin{aligned}
F\big(f_x, f_y, f_z\big) &= \frac{H_1\big(f_x, f_y, f_z\big) H_2{}^*\big(f_x, f_y, f_z\big)}{\sqrt{\big|H_1\big(f_x, f_y, f_z\big) H_2\big(f_x, f_y, f_z\big)\big|}} \\
&= \big|H_1\big(f_x, f_y, f_z\big)\big| \exp\big\{ j\big[\phi_1\big(f_x, f_y, f_z\big) - \phi_2\big(f_x, f_y, f_z\big)\big]\big\}
\end{aligned}
\tag{7}
$$

where $\phi_1(f_x, f_y, f_z)$ and $\phi_2(f_x, f_y, f_z)$, are the phases of $H_1(f_x, f_y, f_z)$ and $H_2(f_x, f_y, f_z)$, respectively. It is seen that

$$\phi_1\big(f_x, f_y, f_z\big) - \phi_2\big(f_x, f_y, f_z\big) = 2\pi\big(uf_x + vf_y + wf_z\big) \tag{8}$$

Finally, a function is obtained by performing another 3D FFT resulting in

$$G(\xi, \eta, \zeta) = \Im\big\{F\big(f_x, f_y, f_z\big)\big\} = \overline{G}(\xi - u, \eta - v, \zeta - w) \tag{9}$$

which is an expanded impulse function located at (u, v, w). This process is carried out for every corresponding pair of subsets. By detecting crests of all these impulse functions, an array of displacement vectors at each and every subset is obtained.

It is well known that in 2D DSP the random error is a function of the subset size, the speckle size, and the amount of decorrelation. It is also true in DVSP. If the displacement between the corresponding subsets is large, the increase of nonoverlapping area would result in an increase of decorrelation giving rise to an enhanced random error [26]. In order to reduce the random errors, a coarse-fine calculation process is adopted. In the coarse calculation, the first integer voxel prediction indicates that the largest size of the subset $(2^p \times 2^p \times 2^p)$ should not exceed the size of the region-of-interest in the reference volumetric image. And thus, the subset with the size $(2^{p-1} \times 2^{p-1} \times 2^{p-1})$ is used, and the corresponding subset in the deformed volumetric image is chosen based on the first integer voxel predicted displacement. By repeating this process, the optimal subset size is obtained for the fine calculation. In this study, we selected 32 voxel $\times 32$ voxel $\times 32$ voxel as the optimal size for the final calculation, and the subset shift was 5 voxels.

Because of the discrete nature of digital volume images, the displacement vectors evaluated from the above coarse-fine calculation process are integral multiples of one voxel. In order to obtain more accurate and sensitive characterization, a sub-voxel investigation of the crest position is needed. To achieve this, we selected a cubic subset with $3 \times 3 \times 3$ voxels surrounding an integral voxel of the crest and a cubic spline interpolation was employed to obtain the interpolated values among the integral voxels in each respective dimension. After interpolation, the cubic subset was enlarged and a new three dimensional array was generated with a size depending on the interpolation interval. The smaller the interval and the bigger the array size give rise to a higher interpolation accuracy. The price to pay, however, is the need for more computational time and more memory space. In practical applications there would be a tradeoff between the two competing needs. By detecting the positions of peak values of the new array, displacements of subvoxel accuracy can be obtained. The interpolation procedure is illustrated schematically in Fig. 3.

3   Strain Estimation

The internal strain tensor ε can be derived from displacement fields. Due to the influence of unavoidable noise contained in the CT images, the displacements thus determined contains discontinuities or noises that are not a feature of the material but a consequence of the discrete nature of the analysis performed. The errors in local displacements may be amplified during the strain computation process. By using the PLS (Point Least-Squares) approach, the errors can be substantially reduced during the process of local fitting, and the strains thus estimated will be more precise [27].

The element of PLS approach is as follows. To compute the local strain tensor of each considered point, a regular cubic box with size of $(2N+1) \times (2N+1) \times (2N+1)$ discrete points surrounding the point of interest is selected. If the strain calculation
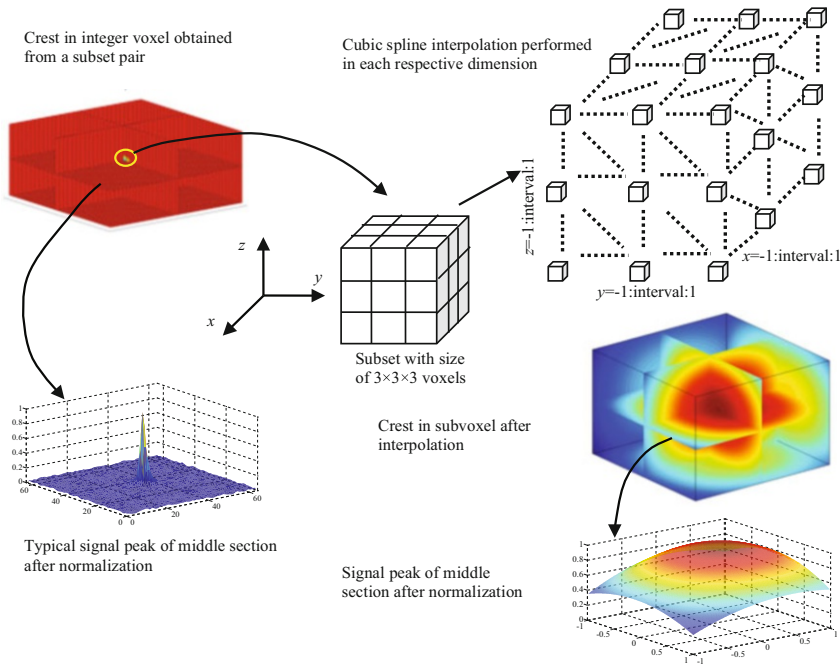
Fig. 3 Schematics showing the interpolation procedure

window is sufficiently small, the displacement in each direction can be reasonably assumed to be linear, and they can be mathematically expressed as

$$
\begin{aligned}
u(x, y, z) &= a_0 + a_1 x + a_2 y + a_3 z \\
v(x, y, z) &= b_0 + b_1 x + b_2 y + b_3 z \\
w(x, y, z) &= c_0 + c_1 x + c_2 y + c_3 z
\end{aligned}
\tag{10}
$$

where $x, y, z = [-N, N]$ are the local coordinates within the strain calculation box, $u(x, y, z)$, $v(x, y, z)$ and $w(x, y, z)$ are displacements directly obtained by the DVSP method; and $a_{i=0,1,2,3}$, $b_{i=0,1,2,3}$ and $c_{i=0,1,2,3}$ are the unknown polynomial coefficients to be determined. With the Least-squares or Multiple Regression Analysis, the unknown coefficients can be estimated. Then, the six Cauchy strain components ε_x, ε_y, ε_z, ε_{xy}, ε_{xz} and ε_{yz} at the interrogated point can be calculated as

$$
\begin{aligned}
\varepsilon_x &= \frac{\partial u}{\partial x} = a_1 & \varepsilon_{xy} &= \frac{1}{2}\left(\frac{\partial v}{\partial x} + \frac{\partial u}{\partial y}\right) = \frac{1}{2}(b_1 + a_2) \\
\varepsilon_y &= \frac{\partial v}{\partial y} = b_2 & \varepsilon_{yz} &= \frac{1}{2}\left(\frac{\partial w}{\partial y} + \frac{\partial v}{\partial z}\right) = \frac{1}{2}(c_2 + b_3) \\
\varepsilon_z &= \frac{\partial w}{\partial z} = c_3 & \varepsilon_{xz} &= \frac{1}{2}\left(\frac{\partial u}{\partial z} + \frac{\partial w}{\partial x}\right) = \frac{1}{2}(a_3 + c_1)
\end{aligned}
\tag{11}
$$

# 4   Experiments & Results

4.1   Experimental Setup

In this study, the main components of the industrial X-Ray computer tomography system consist of a microfocus X-ray source from YXLON (Feinfocus 225 kV), a X-ray detector unit (1024 pixel × 1024 pixel) from PerkinElme (XRD 0822AP 14), and a motorized rotation stage from Newport. The X-ray has a focus with the size of 3 μm × 6 μm, a voltage range of 50–225 kV, and the tube current ranging from 0 to 1440 μA. For each scanning, 720 projections are captured and distributed at equal angles over $360°$. The entire process takes 25 min. For high quality image, more projections can be captured. Based on these projections, the Feldkamp algorithm is used to reconstruct a sequence of slice images, and then a volume image of the specimen is obtained by merging these slice images together.

To test a specimen under load, we designed and built a compact loading setup that would allow the operation of micro-tomography of a specimen under load in situ. By using the loading setup, uniaxial compression, uniaxial tension and 3-point bending experiments can been carried out with different rigs. The setup is enclosed within a cell made of PMMA, which is transparent to X-ray. Mechanical loading is provided by an electric motor with an actuator. A load sensor of 20 kN capacity and 0.002 kN resolution, and a grating scale of 20 mm capacity and 0.001 mm resolution are used to record the load and the displacement, respectively. The CT system and loading setup are shown in Fig. 4.

4.2   A Woven Composite Beam Under 3-Point Bending

The specimen is made of a tri-direction fabric composite material with Advantex SE1500 E-glass filaments and 55% epoxy resin by volume. The filament diameter is

Fig. 4 The Micro-CT system and the loading setup used to record the volumetric image of the specimen at each loading step
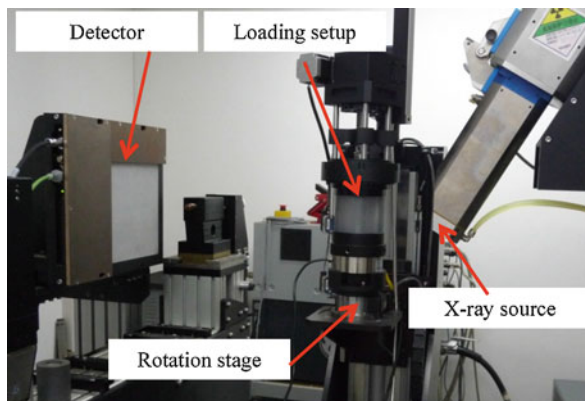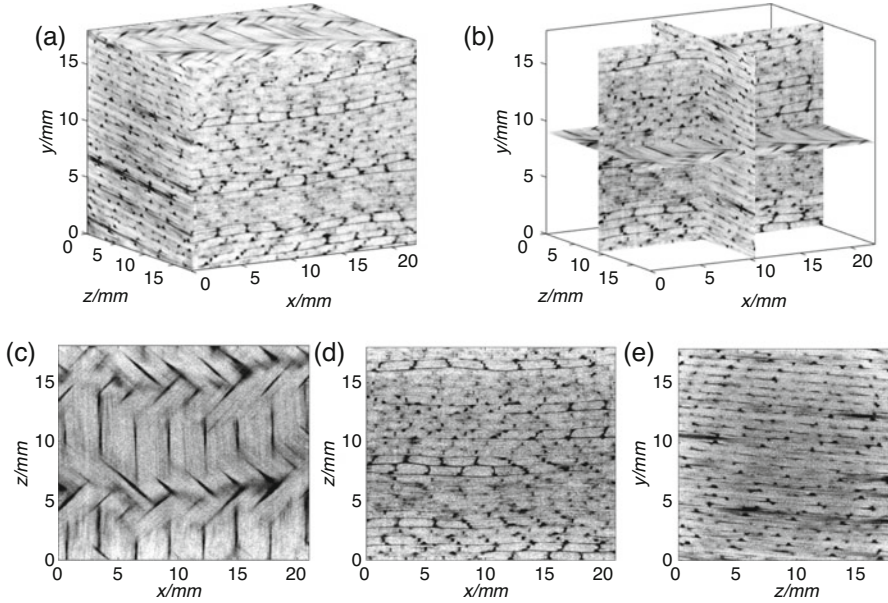
Fig. 5 The woven composite material: (**a**) reconstructed volumetric image based on CT slices; (**b**)- (**e**) Three orthogonal sections of the volumetric image

17 μm, and its density is 2.63 g/cm^3. The fiber orientations are set at +45 °, 0, and −45 ° with respect to the rotation axis. The density of the basic matrix is 1.08 g/cm^3. When applying the DVSP algorithm to composite materials the first issue is whether or not the Micro-CT can capture the minute interior details of the composite material. Figure 5 shows the reconstructed volume image and three orthogonal sections of the woven composite material based on CT slices by using the Micro-CT system. Even though the density of the filament is more than twice that of the matrix, the size of filament is small, and beyond the scanning resolution of the CT system. Therefore, we cannot detect the filament from the slice image. However, there are a lot of pores with low gray value as shown in the images. These internal meso-structures are of sufficient details that they can be treated as 3D speckles. Thus the algorithm of DVSP can be effectively applied.

The dimension of the beam specimen for 3-point bending is 38.8 (L) mm × 18.8 (H) mm × 9.0 (T) mm, while the span between two supports is 30.0 mm. The beam was loaded with step-wise increments until failure appears via visual observation. There were 11 loading steps [28]. After each loading step the specimen was scanned by the CT system. The load-displacement curve is shown in Fig. 6(a). In each step, a reconstructed volume image with size of 900 voxel × 250 voxel × 361 voxel was obtained; and the voxel resolution is 45 μm × 45 μm × 45 μm. Figure 6(b) shows the reconstructed CT image of the specimen at loading Step 1. No damage of the material is discernable from surface inspection of the specimen up to the loading
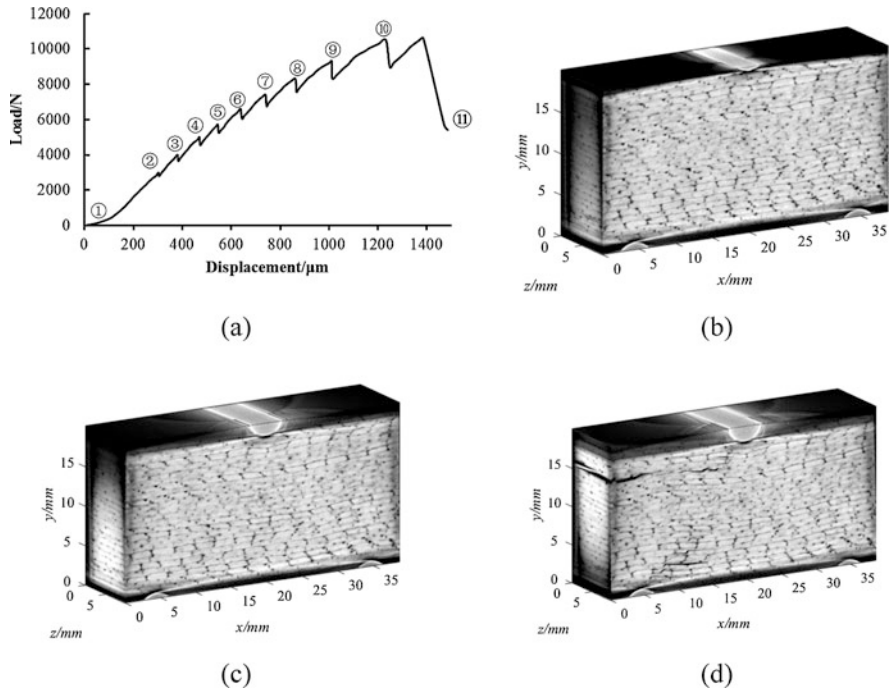
Fig. 6 Loading/displacement curve and reconstructed volume images: (**a**) the load-displacement curve (**b**) the volume image of Step 1 (**c**) the volume image of Step 10 (**d**) the volume image of Step 11

Step 10, as shown in Fig. 6(c). But micro cracks are clearly visible on the surface of the specimen after loading Step 11 as shown in Fig. 6(d).

The volume image of Step 1 is treated as the reference volume image, and volume images of subsequent steps (Step 2-Step 10) are "compared" to the reference volume image via the DVSP algorithm. The coarse-fine calculation process was applied, the final subset size was 32 voxel × 32 voxel × 32 voxel, and the subset shift was 5 voxels.

In Fig. 7, displacement fields of three transverse sections at Step 10 with F = 10,500 kN are depicted. Strain fields were then calculated from the displacement data. The size of the calculation cubic element was $31 \times 31 \times 31$ points, and the shift step was 5 points. In Fig. 8, the strain ε_{xx}, ε_{yy}, ε_{zz} and ε_{xy} of the middle longitudinal section in Step 7, Step 9 and Step 10 are shown, respectively. It is noted that the internal heterogeneity of the woven composite had manifested itself vividly on the strain distributions. The distribution of the normal strain ε_{xx} indicates the periodic distributions of the matrix and fiber, whereas the distribution of normal strain ε_{yy} reflects the layered characteristics of the material. The distribution of the shear strain ε_{xy} as the load increases clearly indicates where the failure would eventually occur, as shown in in Fig. 6(d) at loading Step 11.

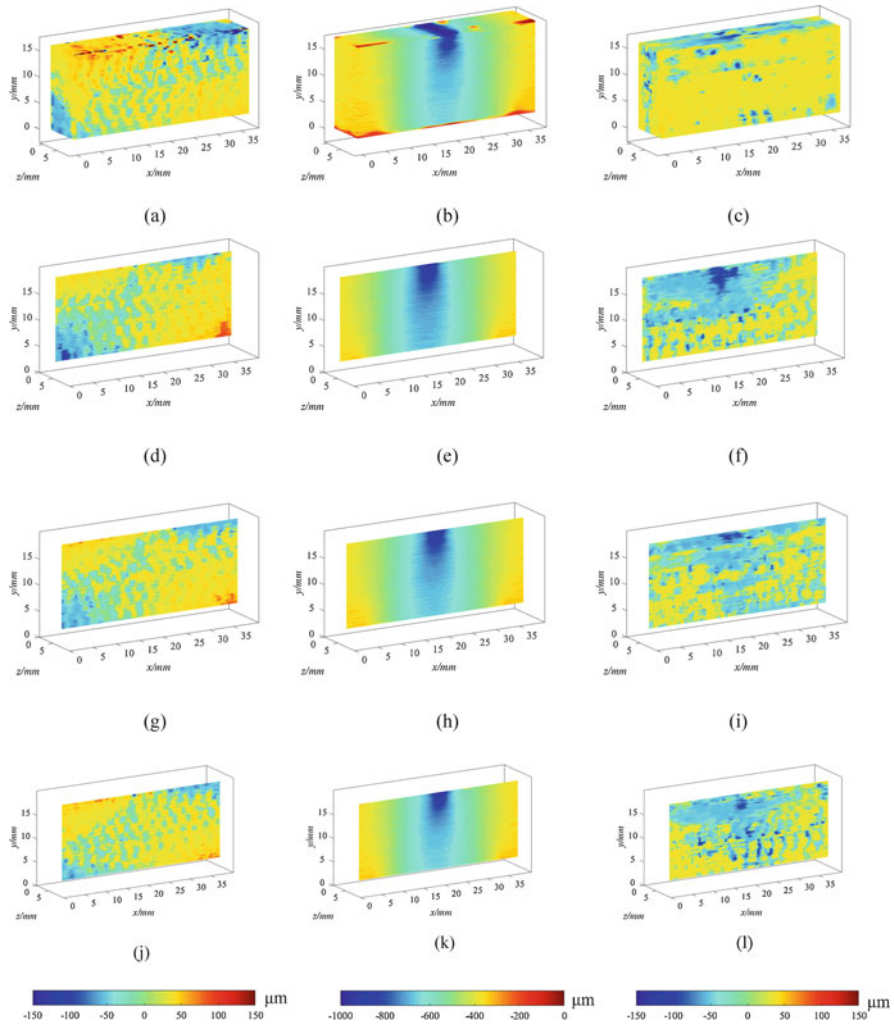**Fig. 7** Displacement fields of the specimen at loading Step 10; (**a**)-(**c**) u, v, w fields of the whole specimen within the cropped region; (**d**)-(**f**) u, v, w fields of the transverse section at $z = 2.25$ mm; (**g**)-(**i**) u, v, w fields of the transverse section at $z = 4.50$ mm; (**j**)-(**l**) u, v, w fields of the transverse section at $z = 6.75$ mm

4.3 A Woven Composite Beam With a Prepared Slot Under 3-Point Bending

The experiment of a woven composite beam with a prepared slot under 3-point bending was conducted. The material of the beam is the same as that in Sect. 4.2. The dimension of the specimen is 39 (L) mm × 18 (H) mm × 8.5 (T) mm, and the size of
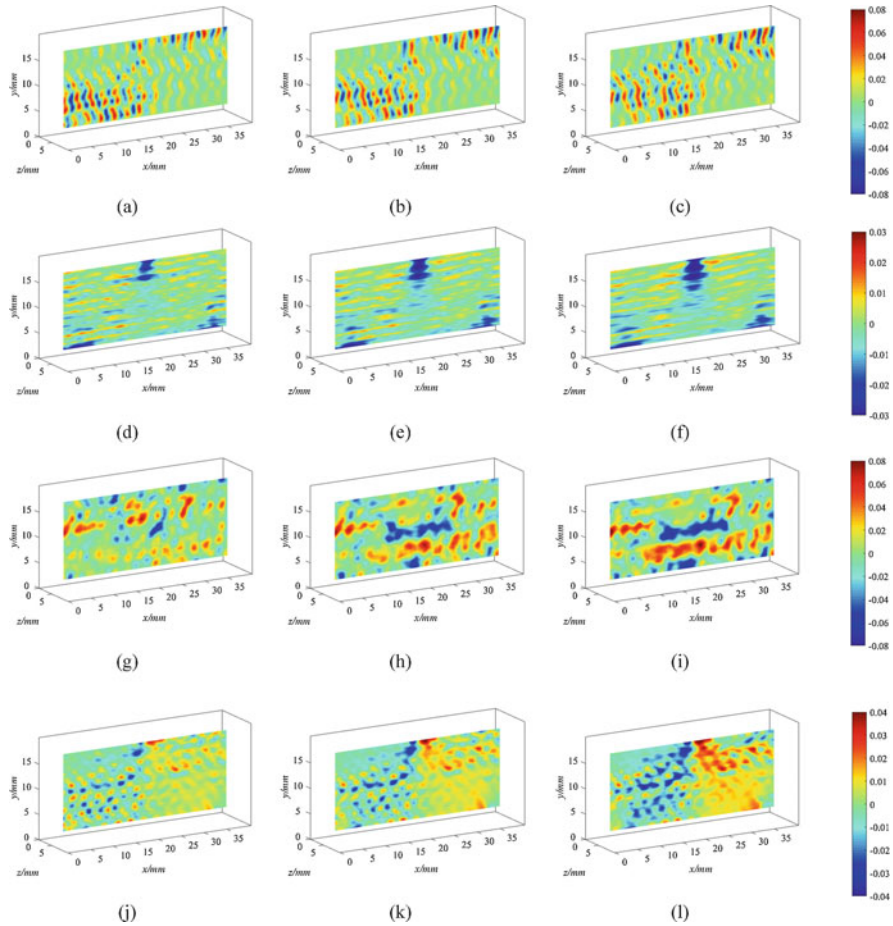
Fig. 8 Strain distribution of the middle longitudinal section at $z = 4.50$ mm under different loadings steps: (**a**)-(**c**) ε_{xx} at Step 7, Step 9 and Step 10, respectively; (**d**)-(**f**) ε_{yy} at Step 7, Step 9 and Step 10, respectively; (**g**)-(**i**) ε_{zz} at Step 7, Step 9 and Step 10, respectively; (**j**)-(**l**) ε_{xy} at Step 7, Step 9 and Step 10, respectively

the slot is 3.60 mm $\times$ 0.68 mm. The span between two supports is 30.0 mm. The load was applied incrementally in 10 steps. The load-displacement curve is shown in Fig. 9(a). The size of the reconstructed volume image in each step is 960 voxel $\times$ 260 voxel $\times$ 424 voxel, and the voxel resolution is also 45 μm $\times$ 45 μm $\times$ 45 μm. Comparing Fig. 6(a) with Fig. 9(a), the loading capacity of the specimen with a slot is reduced due to the weakening effect of the slot. The maximum loading of the specimen with a slot was 8400 N, whereas that of the specimen without a slot was 11,700 N. From Figs. 6(d) and 9(d), it is noted that there is a delamination crack on the left upper region of those two specimens. In the maximum shear strain region of the specimen without a slot, delamination was the failure mode, whereas for the specimen with a slot, cracking was the failure mode.
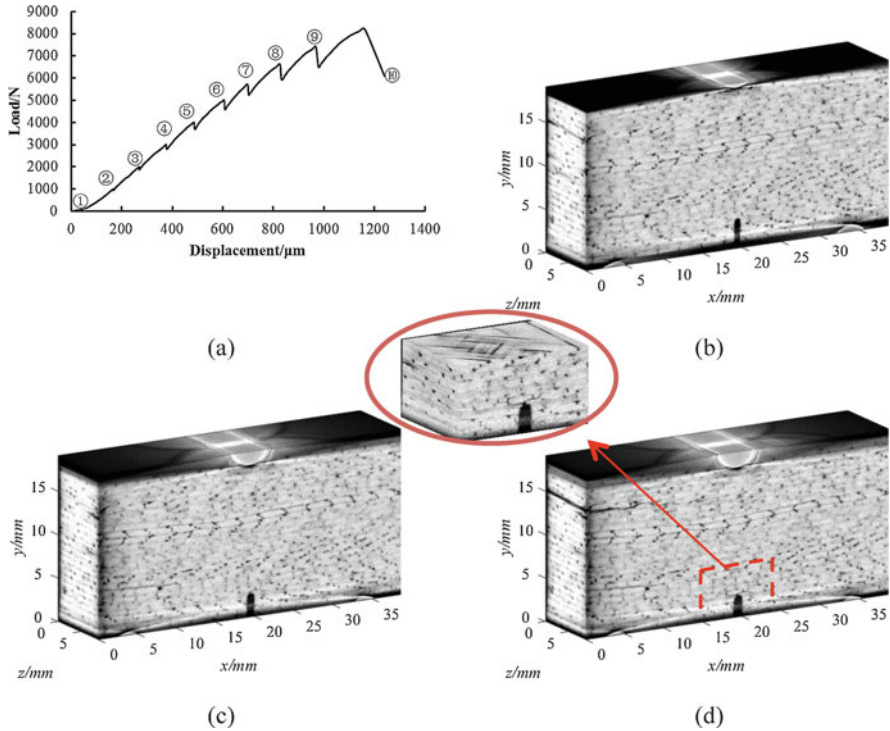
Fig. 9 Loading/displacement curve and reconstructed volume images: (**a**) load-displacement curve; (**b**) volume image of Step 1; (**c**) volume image of Step 9; (**d**) volume image of Step 10

The volume image of Step 1 was treated as the reference volume image, and volume image of subsequent steps (Step 2-Step 9) were "compared" to the reference volume image using the DVSP algorithm. The coarse-fine calculation process was applied, the final subset size was 32 voxel × 32 voxel × 32 voxel, and the subset shift was 5 voxels.

In Fig. 10, 3D displacement fields of the specimen and three transverse sections at Step 9 with F = 7400 N are depicted. Periodic patterns in the displacement field due to the periodic structure of the specimen are also found. Figure 11(a), 11(b) and 11(c) show images of the region near the slot in different sections at Step 10. Corresponding to these regions, the u and v displacement fields of Step 9 are plotted as shown in Fig. 11(d), 11(e), 11(f), 11(g), 11(h) and 11(i), ε_{xx} and ε_{xy} strain fields of Step 9 are plotted as shown in Fig. 11(j), 11k, 11(l), 11(m), 11(n) and 11(o). Strain concentrations are clearly indicated in various locations. Corresponding to the zone of cracks, there are higher strain values in ε_{xy} fields.
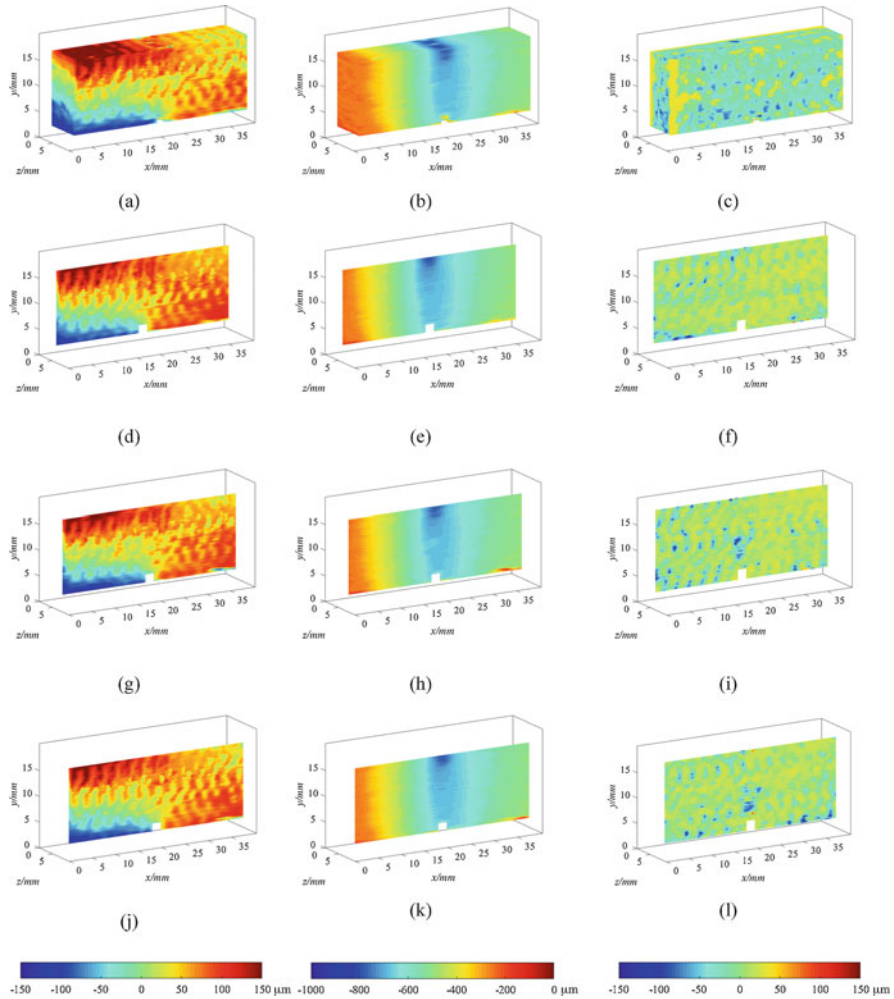
Fig. 10 Displacement fields of the specimen at loading Step 9; (**a**) – (**c**) u, v, w fields of the whole specimen; (**d**) – (**f**) u, v, w fields of the transverse section at $z = 2.00$ mm; (**g**) – (**i**) u, v, w fields of the transverse section at $z = 4.25$ mm; (**j**) – (**l**) u, v, w fields of the transverse section at $z = 6.50$ mm

4.4 A Woven Sandwich Beam Under 3-Point Bending

The size of the sandwich beam is 50.0 mm × 20.0 mm × 33.0 mm, the thickness of the face sheet is 3.8 mm, and the span between two supports is 30.0 mm. The face sheet is made of E-glass vinyl ester (EVE) composite with the fiber woven into a quasi-isotropic layout: [0/45/90–45]$_s$. The fibers are made of a 0.61 kg/m^2 areal density plain weave. Ashland Derakane Momentum 8084 resin are used as the matrix material. The two face sheets are of identical layups and materials. The
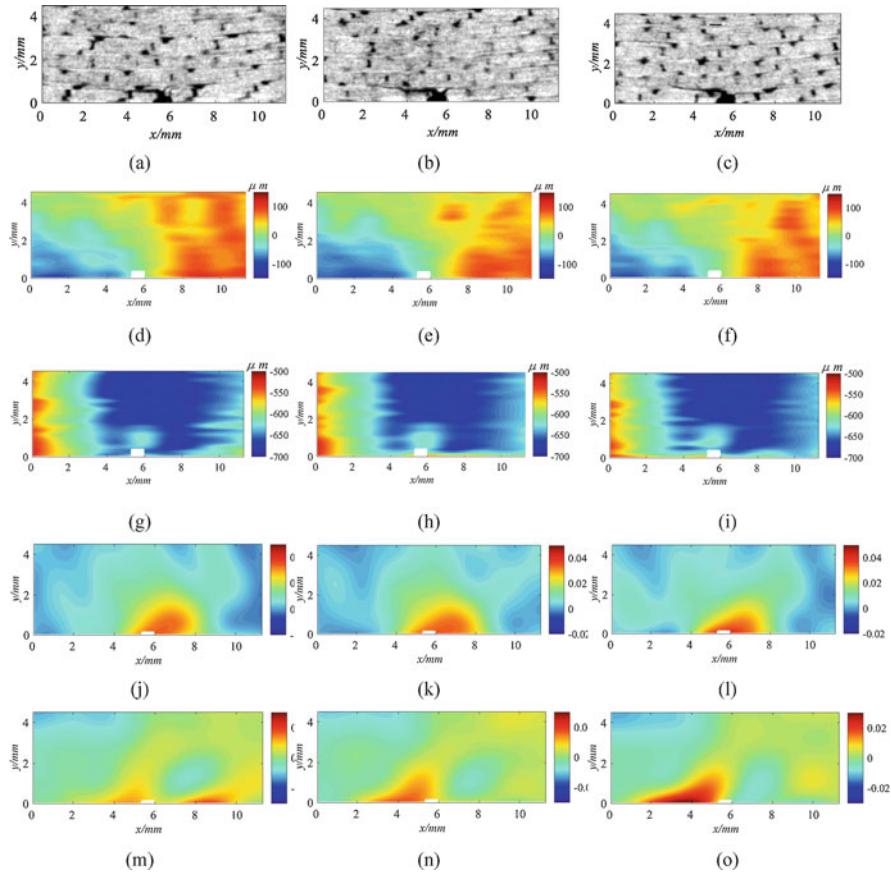
Fig. 11 Displacement and strain distributions of Step 9 near the slot in different sections (**a**)section along $z = 2.00$ mm of Step 10; (**b**) section along $z = 4.25$ mm of Step 10; (**c**) section along $z = 6.25$ mm of Step 10; (**d**) u field of (**a**); (**e**) u field of (**b**); (**f**) u field of (**c**); (**g**) v field of(**a**); (**h**) v field of (**b**); (**i**) v field of (**c**); (**j**) ε_{xx} field of (**a**); (**k**) ε_{xx} field of (**b**); (**l**) ε_{xx} field of (**c**); (**m**) ε_{xy} field of (**a**); (**n**) ε_{xy} field of (**b**); (**o**) ε_{xy} field of (**c**)

core material is made of Corecell™ P600 styrene foam [29]. The whole loading process is divided into 6 steps [30]. In each step, the specimen was CT scanned and a volumetric image with 890 voxel × 360 voxel × 530 voxel was reconstructed, and the physical size of a voxel is 55 μm × 55 μm × 55 μm. The volume image of the specimen and the loading history are shown in Fig. 12.

Since the length of the beam is rather short, at the end of the loading history we did not observe any shear crack in the foam core or along the interface of face sheet and core. The volume image of Step 1 was designated as the reference image, whereas the subsequent images were the deformed images. By applying the DVSP algorithm, the displacement contours of u, v, w of the core after each incremental loading from Step 2 to Step 5, were calculated. The core region with the size of
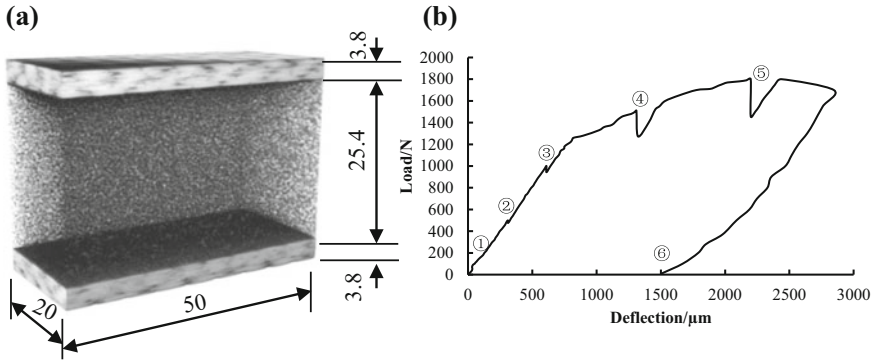
Fig. 12 3D image and loading history: (**a**) Reconstructed 3D image of the specimen; (**b**) loading history

890 voxel × 360 voxel × 430 voxel was boxed in for the calculation. The coarse-fine calculation process was applied, the final subset size was 32 voxel × 32 voxel × 32 voxel, and the subset shift was 5 voxels. The displacement contours of the core under different loadings are depicted in Fig. 13. The first three patterns, Figs. 13(a), 13(b) and 13(c), show clearly the characteristic deformation of a short beam under 3-point bending. The distributions of u and v fields are self-explanatory. The w-field shows a barrel-like bulging of the central part of the beam, a pattern similar to the deformation of a short square column under compression with the movement of both ends constrained. As the loading increases the displacement fields lose some of the symmetry as shown in subsequent pictures in Fig. 13. This is because the loading was not exactly symmetrical, a common occurrence in a typical testing arrangement.

In the process of the strain calculation, the size of the calculation cubic box is 31 × 31 × 31 points, and the shift step is 5 points. Since a sandwich beam under bending tends to fail in the form of shear failure of the core, we only calculated the in-plane shear strain distributions, and only at loading steps 3, 4, and 5 with loads being 1000 N, 1500 N, and 1800 N, respectively. As depicted in Fig. 14, ε_{xy} contours of the entire core within the cropped region for the three loads are shown in Figs.14(a), 14(b), and 14(c), respectively. Figures 14(d), 14(e), and 14(f) depict the in-plane shear strain distributions in the plane of $z = 5.875$ mm; Figs. 14(g), 14(h) and 14(i) depict the shear strains in the plane of $z = 10.00$ mm, and Figs. 14(j), 14(k) and 14(l) depict the shear strains in the plane of $z = 14.12$ mm under the same three different loadings, respectively. It is clearly seen that shear strains are localized along two 45 degree bands fanning out from the point where the concentrated load was applied. If the sandwich beam were longer, it is believed that failure would probably occur along these two shears bands. From the patterns shown in Fig. 14(c), it is reasonable to suspect that failure would probably initiate from the interior of the foam core.
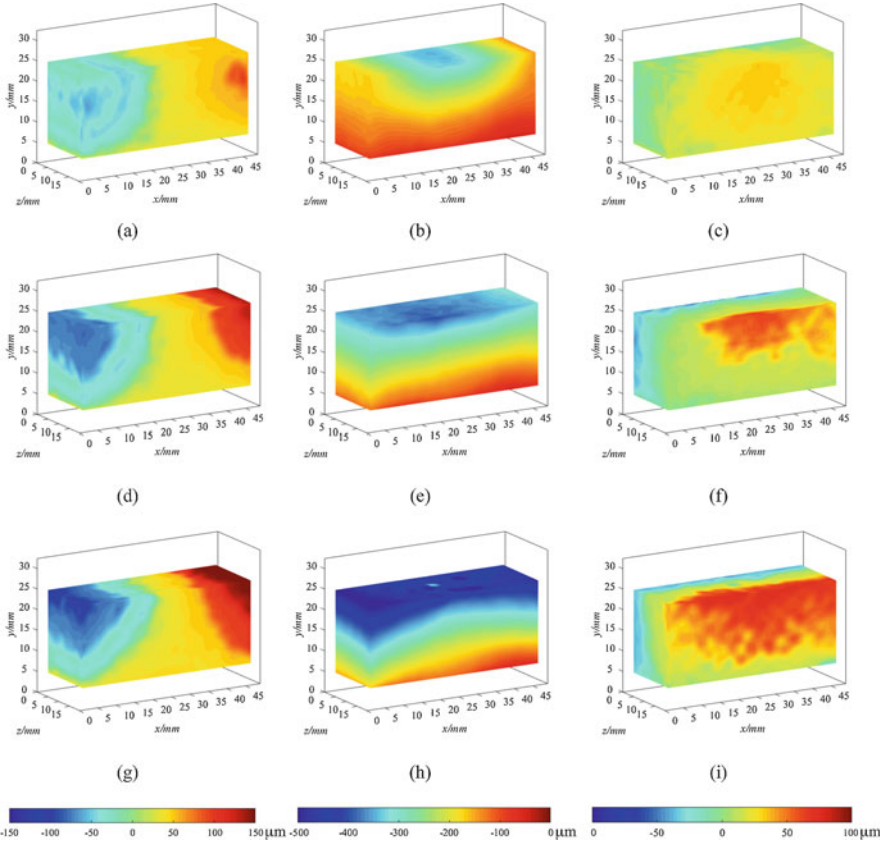
Fig. 13 Displacement distribution of the core under different loadings: (**a**)-(**c**) *u*, *v* and *w* fields, respectively, at Step 3 with loading 1000 N; (**d**)-(**f**) *u*, *v* and *w* fields, respectively, at Step 4 with loading 1500 N; (**g**)-(**i**) *u*, *v* and *w* fields, respectively, at Step 5 with loading 1800 N

5 Discussion

5.1 The Effect of Subset Size

One of the important features of the DVSP method is the fact that the interior meso- or microstructures of the specimen material are treated as volumetric speckles. These structural features tend to vary from material to material and from region to region. They don't form ideal speckle patterns. Thus, it is important that the size of the subset be selected judiciously when applying DVSP. As a demonstration of the size effect of subset, we cropped a cubic block with 200 voxel × 200 voxel × 200 voxel from each of the two volume images of the two tested materials as shown in Figs. 15 (a) and 16(a). These two images are defined as the reference volume images, whereas the "deformed" volume images are obtained by the Fourier shifting method. For
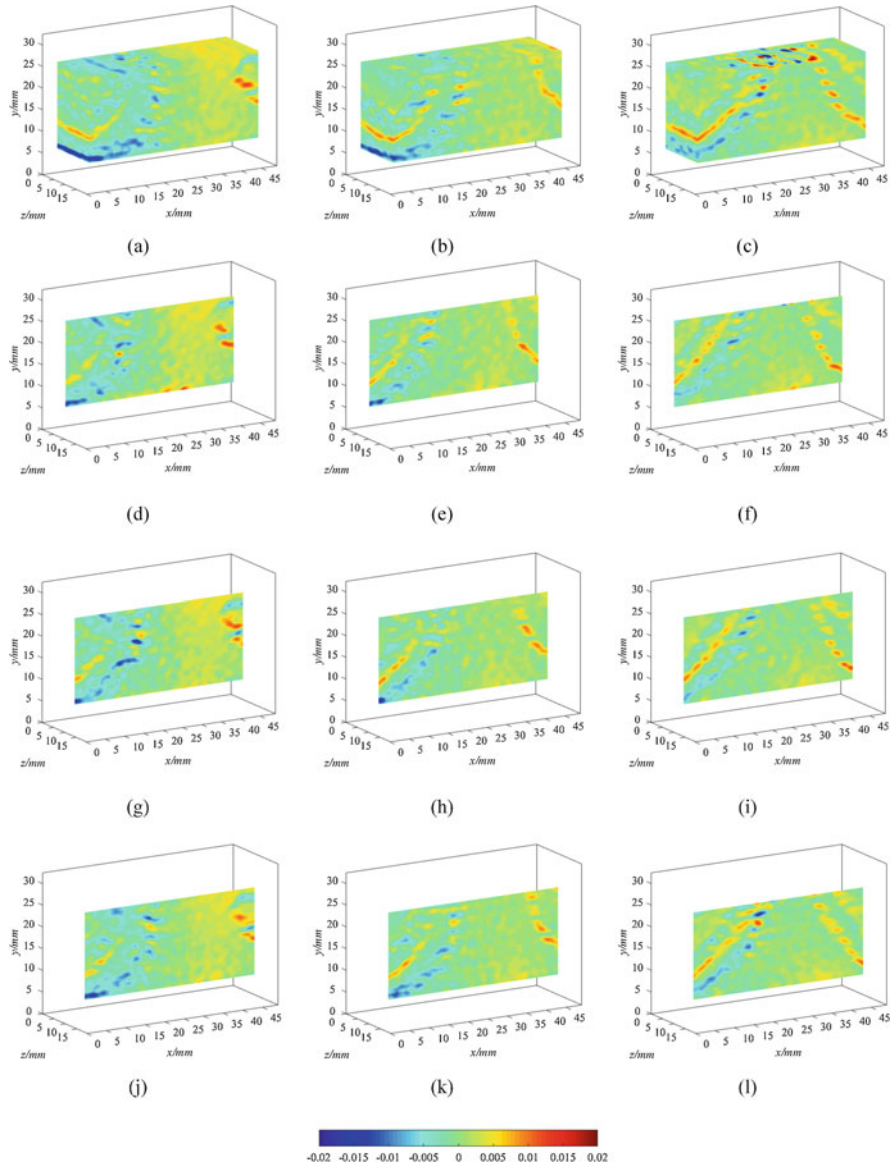
Fig. 14 Shear strain distribution of the core under different loadings: (**a**)-(**c**) ε_{xy} field of the whole core under loadings of 1000 N, 1500 N and 1800 N, respectively; (**d**)-(**f**) ε_{xy} fields of the longitudinal section at $z = 5.875$ mm under loadings of 1000 N, 1500 N and 1800 N, respectively; (**g**)-(**i**) ε_{xy} fields of the longitudinal section at $z = 10$ mm under loadings of 1000 N, 1500 N and 1800 N, respectively; (**j**)-(**l**) ε_{xy} fields of the longitudinal section at $z = 14.125$ mm under loadings of 1000 N, 1500 N and 1800 N, respectively
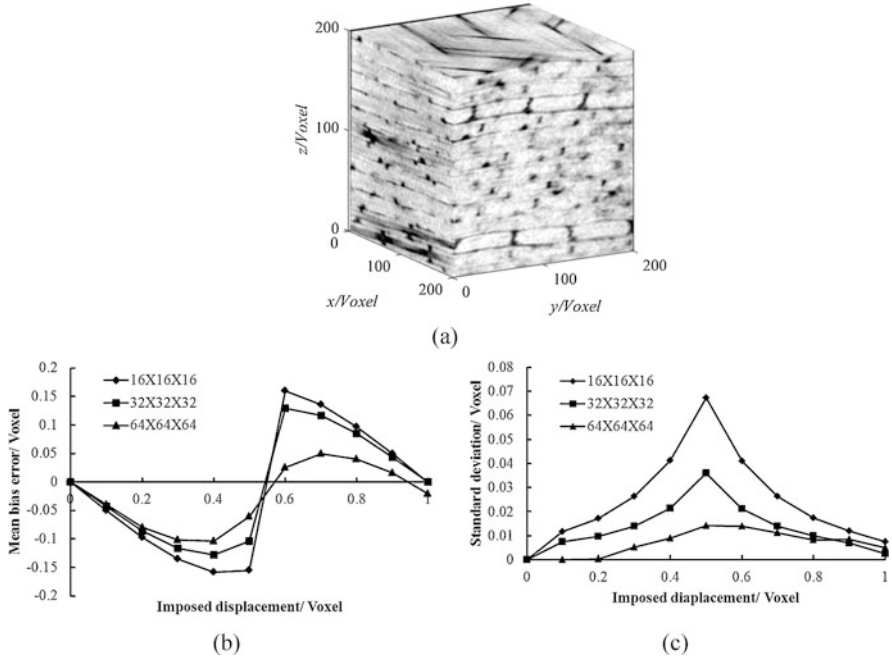
Fig. 15 Accuracy of DVSP on the woven composite specimen: (**a**) a cubic volume image of the woven composite specimen; (**b**) mean bias error of the displacement; (**c**) standard deviation of the displacement

every reference volume image, ten different "deformed" volume images with sub-voxel rigid body translation ranging from 0.1 to 1.0 voxel, respectively, along the z direction were obtained. In the fine calculation, the subset size with 16 voxel $\times$ 16 voxel $\times$ 16 voxel, 32 voxel $\times$ 32 voxel $\times$ 32 voxel and 64 voxel $\times$ 64 voxel $\times$ 64 voxel, respectively, were used. And the subset shift is 5 voxels. The resulting mean bias errors and the standard deviation errors of displacements are shown in Figs. 15(b), (c) and 16(b), (c), respectively. It is seen that the larger the subset size, the smaller the resulting error. However, as the subset size increases, fewer independent measurement points can be obtained which will influence the resolution of strain calculation [31]. It is noted that the meso-structure of the foam core is much more uniform than that of the woven composite, thus gives rise to better accuracies.

In the DVSP theory, the subset is assumed to be rigid. In reality there is deformation and rotation of the material within the subset. While by increasing the subset size results in better accuracy of DVSP, the errors caused by ignoring the deformation and rotation of the material within the subset tend to increase too. To estimate the effects of deformation within the subset on DVSP, we used a quadratic displacement model test [32]. The above blocks with 200 voxel $\times$ 200 voxel $\times$
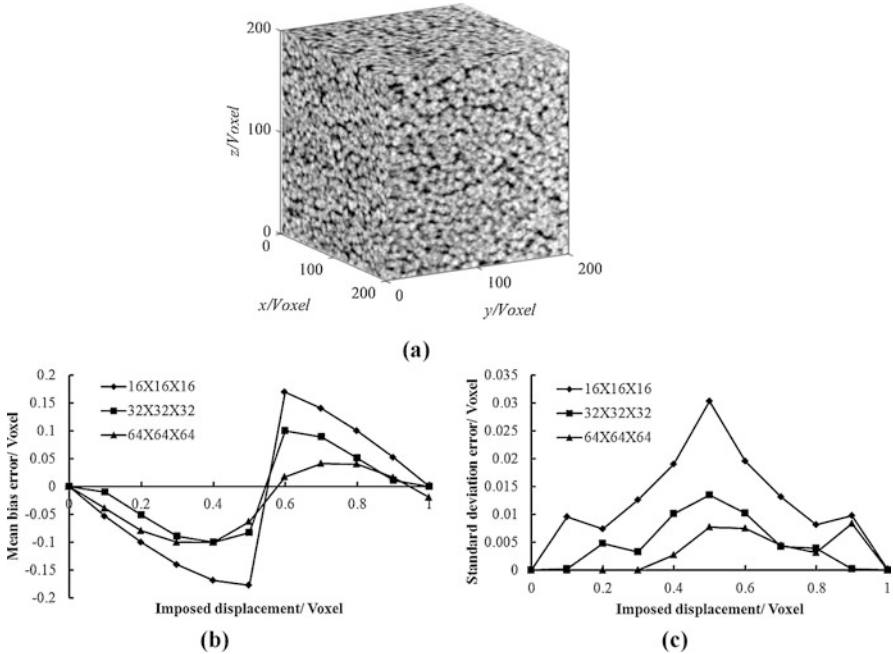
Fig. 16 Accuracy of DVSP on the core of the sandwich specimen: (**a**) a cubic volume image of the woven composite specimen; (**b**) mean bias error of the displacement; (**c**) standard deviation of the displacement

200 voxel was again used as the reference volume image, whereas the "deformed" volume image was obtained as follow: the block was given a rigid displacement of 2 voxels along the z axis, and then divided into three regions along the z axis. Region 1 ($1 \leq z < 68$ voxels) has a linear displacement field with strain $\varepsilon_1 = -0.1\%$; Region 2 ($68 \leq z < 134$ voxels), has a quadratic displacement with strain varying from $\varepsilon_1 = -0.1\%$ to $\varepsilon_2 = 0.5\%$; and Region 3 ($134 \leq z < 200$ voxels) has a linear displacement field with strain $\varepsilon_2 = 0.5\%$. The displacement fields were calculated by using DVSP with different subset sizes having 16 voxel ×16 voxel ×16 voxel, 32 voxel × 32 voxel × 32 voxel and 64 voxel × 64 voxel× 64 voxel, respectively, and all with 5 voxels shift. The displacement and strain were calculated and are depicted in Fig. 17. It is noted that the deformation in subset do result in noticeable error. In Region 1 and Region 2, smaller subsets capture the solution more accurately, whereas in Region 3, larger subset has better results. For all these three regions, the optimal subset size is 32 voxel × 32 voxel × 32 voxel. In order to reduce the influence of subset deformation, one can use the iterative least-squares method [27], but iterative procedures tend to increase the implementation complexity resulting in more computational expenses.

The deformation between the reference subset and the corresponding deformed subset would cause the correlation coefficient to decrease. We imposed a set of uniform deformation with strains from 0.1% to 1% with the interval 0.1% on the
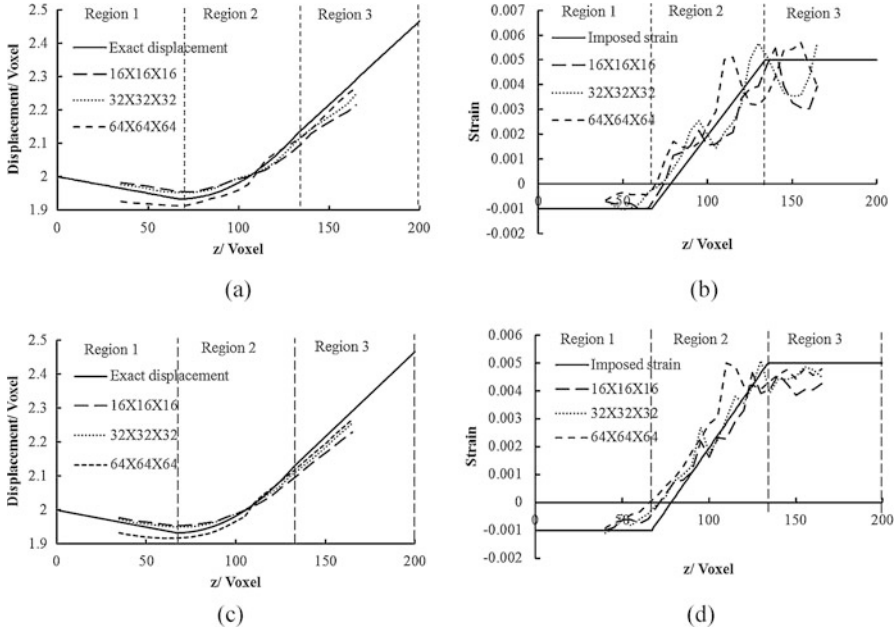
Fig. 17 Calculated results of DVSP in the quadratic displacement test: (**a**) Exact displacement and displacement curves of the woven composite with different subset sizes; (**b**) Imposed strain and calculated strain curves of the woven composite with different subset sizes; (**c**) Exact displacement and displacement curves of the core in the sandwich with different subset sizes; (**d**) Imposed strain and calculated strain curves of of the core in the sandwich with different subset sizes

woven composite block shown in Fig. 15(a) to obtain the deformed volume images, and calculated the correlation coefficients between the reference image and the deformed image. The subset size was 32 voxel × 32 voxel × 32 voxel, and the subset shift was 5 voxels. The correlation coefficient curve with strain is shown in Fig. 18(a). The coefficient decreases in a nearly quadratic function as the strain increases, and the standard deviation rises as the strain increases. When the strain is 1%, the coefficient is 82.2%, and the standard deviation is 0.12. In Fig. 18(b), the curve shows that the influence of the displacement is more than one voxel on the correlation coefficient. When the displacement is 8 voxels, one fourth of subset, the coefficient drops 53.4%, and standard deviation to 0.11. Figures 18(c) and 18(d) are typical 2D normalized impulse function distributions under the influence of deformation and integer voxel displacement, respectively. When the signal-to-noise-ratio decreases, it would affect the detection of the crest of the impulse functions. For the purpose of increasing signal-to-noise-ratio, we carried out a coarse-fine calculation process. In the coarse calculation, integer voxel displacement evaluation is more robust with the large subset size, and strain calculation resolution can be supported in the fine calculation with the small subset size.
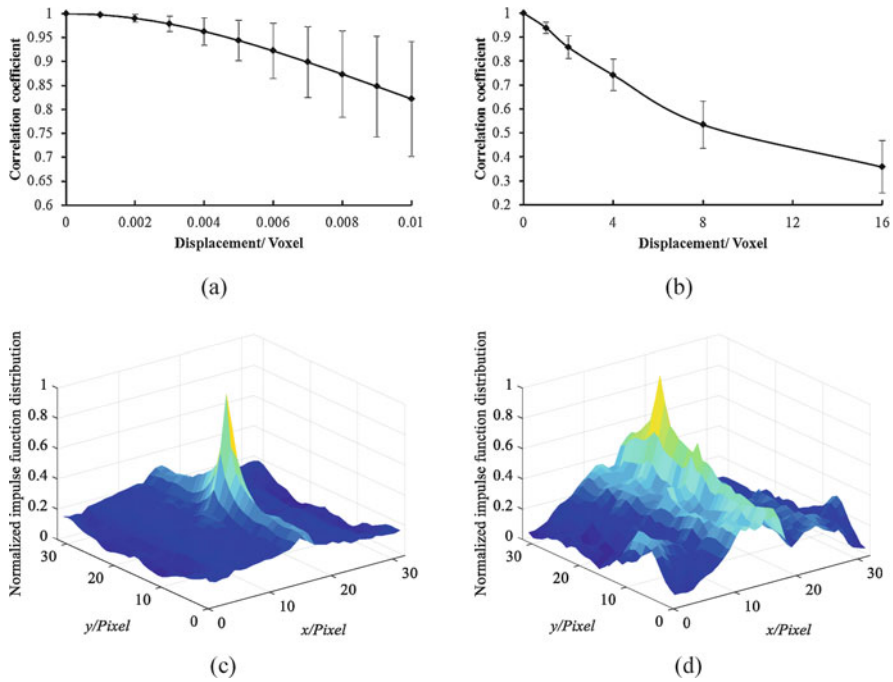
Fig. 18 Influence on correlation coefficient of the deformation and the integer voxel displacement: (**a**) the curve of correlation coefficient with different strain deformation; (**b**) the curve of correlation coefficient with different integer voxel displacement; (**c**) a 2D correlation coefficient distribution with strain deformation influence; (**d**) a 2D correlation coefficient distribution with 8 voxels displacement influence

5.2 Influence of Artifacts in CT Images

CT slice images are reconstructed with an appropriate mathematical algorithm from the different angular radiographic projections. The non-uniformity of detector elements, the polychromatic nature of the X-ray, the imperfect motion of the rotation stage, the temperature variation of the X-ray tube, and the possible rigid body motion of the specimen will all give rise to different artifacts, such as streak, ring, and beam hardening [33]. These artifacts will influence the measurement results. To analyze the effects of artifacts of the micro X-ray CT system, we took two consecutive scans of a woven composite specimen with identical settings and without moving (other than the tomographic rotation) or deforming the sample and designated them as Scans 1 and 2, respectively. Noise and artifacts of the system were present in the reconstructed image of both scans. Two volumetric images with a size of 200 voxel × 200 voxel × 200 voxel were cropped from the reconstructed images. The physical size of a voxel was 42 μm × 42 μm × 42 μm.

We defined the volumetric images of Scans 1 and 2 as the reference image and deformed volumetric image, respectively. We then assess the influence of artifacts in

Table 1 Least squares fit of the displacements to the exact solution with rigid body translation and small angle rotation

u_{rigid}	v_{rigid}	w_{rigid}	θ_x	θ_y	θ_z
0.74	0.89	0.60	1.58×10^{-4}	2.22×10^{-4}	1.93×10^{-4}

CT images using the DVSP algorithm with subvoxel shifting. The average measured displacements are $u = 0.75$ voxels, $v = 0.83$ voxels, and $w = 0.69$ voxels, and the standard deviation errors are 0.12 voxels, 0.18 voxels and 0.20 voxels, respectively. All of the measured displacements are greater than the standard deviation errors, indicating that some motion occurred between scans due to physical perturbations in the CT system. Because there are real noise and artifacts in the volumetric images of Scans 1 and 2, the above results can depict the uncertainty of the algorithm in its application.

As a more accurate alternative to fitting just rigid body movements, a least squares fit was used to calculate rigid body translations and rotations, assuming small angles [34], i.e.

$$
\begin{aligned}
u_{\mathrm{rigid}} + \theta_z Y - \theta_y Z &\cong U \\
v_{\mathrm{rigid}} - \theta_z X + \theta_x Z &\cong V \\
w_{\mathrm{rigid}} + \theta_y X - \theta_x Y &\cong W
\end{aligned}
\tag{12}
$$

where θ_x, θ_y, and θ_z are the rotations about the x, y, and z axes, respectively, and X, Y, Z and U, V, W are the vectors of the x, y, z coordinates and u, v, w displacements, respectively, for all of the correlation points. The results are shown in million. There are rigid body translations similar to the average measured displacements values. Thus, when compared with the volumetric image of Scan 1, the volumetric image of Scan 2 incurred noticeable rigid body translations in all three directions but with small rotations (Table 1).

6   Conclusion

This study describes in detail a new experimental method, called DVSP (Digital Volumetric Speckle Photography), that is capable of probing the interior 3D deformation field of composites. A woven composite beam, a woven composite beam with a prepared slot and a sandwich composite beam are selected to demonstrate the technique's unique capability. DVSP takes advantage of modern industrial X-ray CT's capability to obtain a 3D volume image of a solid object in digital form. The solid's internal meso/micro structures are treated as 3D volumetric speckles. The digitized volume image is subdivided into an array of cubic voxels of certain predetermined size and processed using a 2-step 3D FFT algorithm. The result is a 3D array of displacement vectors, from which the strain field can be calculated using an appropriate strain-displacement relation. Better results can be obtained with a

higher power X-ray, which has a better resolution, a more rugged CT system and a more efficient software. Even with the current state of art, we believe DVSP can contribute significantly to the understanding of thick composite's 3D effects and failure mechanism.

References

1. Butters JN, Leendertz JA (1971) Speckle pattern and holographic techniques in engineering metrology. Opt Laser Technol 2:26–30
2. Leendertz JA (1970) Interferometric displacement measurement on scattering surfaces utilizing speckle effect. J Phys 3:214–218
3. Daniel IM, Rowlands RE, Post D (1973) Strain analysis of composites by moiré methods. Exp Mech 13:246–252
4. Post D, Han B, Ifju PG (1994) High sensitivity Moiré. In: Experimental analysis for mechanics and materials. Springer, Berlin
5. Chang S, Hong D, Chiang FP (2004) Macro and micro deformations in a sandwich foam core. Compos Part B 35:503–509
6. Fathi A, Keller JH, Altstaedt V (2015) Full-field shear analyses of sandwich core materials using digital image correlation (DIC). Compos Part B 70:156–166
7. Pollock P, Yu L, Sutton MA, Guo S, Majumdar P, Gresil M (2012) Full-field measurements for determining orthotropic elastic parameters of woven glass-epoxy composites using off-axis tensile specimens. Exp Tech 38:61–71
8. Gre'diac M (2004) The use of full-field measurement methods in composite material characterization: interest and limitations. Compos Part A 35:751–761
9. Ju Y, Wang L, Xie HP, Ma GW, Mao LT, Zheng ZM, Lu JB (2017a) Visualization of the three-dimensional structure and stress field of aggregated concrete materials through 3D printing and frozen-stress techniques. Constr Build Mater 143:121–137
10. Ju Y, Wang L, Xie HP, Ma GW, Zheng ZM, Mao LT (2017b) Visualization and Transparentization of the structure and stress field of aggregated Geomaterials through 3D printing and Photoelastic techniques. Rock Mech Rock Eng 50:1383–1407
11. Sciammarella CA, Chiang FP (1964) The moire method applied to three-dimensional elastic problems. Exp Mech 4(11):313–319
12. Asundi A, Chiang FP (1982) Theory and application of white light speckle methods. Opt Eng 21:570–580
13. Dudderar TD, Simpkins PG (1982) The development of scattered light speckle metrology. Opt Eng 21:396–399
14. Schilling PJ, Karedla BR, Tatiparthi AK, Verges MA, Herrington PD (2005) X-ray computed microtomography of internal damage in fiber reinforced polymer matrix composites. Compos Sci Technol 65:2071–2078
15. Nikishkov Y, Airoldi L, Makeev A (2013) Measurement of voids in composites by X-ray computed tomography. Compos Sci Technol 89:89–97

16. Roux S, Hild F, Viot P, Bernard D (2008) Three-dimensional image correlation from X-ray computed tomography of solid foam. Compos Part A 39:1253–1265
17. Brault R, Germaneau A, Dupré JC, Doumalin P, Mistou S, Fazzini M (2013) In-situ analysis of laminated composite materials by X-ray micro-computed tomography and digital volume correlation. Exp Mech 53:1143–1151
18. Lecomte-Grosbras P. R'ethor'e J. Limodin N. Witz J.-F. Brieu M (2015) Three-dimensional investigation of free-edge effects in laminate composites using X-ray tomography and digital volume correlation. Exp Mech 55:301–311
19. Chiang FP, Mao LT (2015) Development of interior strain measurement techniques using random speckle patterns. Meccanica 50:401–410
20. Chen DJ, Chiang FP, Tan YS, Don HS (1993) Digital speckle-displacement measurement using a complex spectrum method. App Opt 32:1839–1849
21. Chiang FP (2009) Super-resolution digital speckle photography for micro/nano measurements. Opt Lasers Eng 47:274–279
22. Mao LT, Chiang FP (2016) 3D strain mapping in rocks using digital volumetric speckle photography technique. Acta Mech 227:3069–3085
23. Mao LT, Hao N, An LQ, Chiang FP, Liu HB (2015) 3D mapping of carbon dioxide-induced strain in coal using digital volumetric speckle photography technique and X-ray computer tomography. Int J Coal Geol 147-148:115–125
24. Mao LT, Yuan ZX, Yang M, Liu HB, Chiang FP (2019) 3D strain evolution in concrete using in situ X-ray computed tomography testing and digital volumetric speckle photography. Measurement 133:456–467
25. Sjodahl M (1997) Accuracy in electronic speckle photography. App Opt 36:2875–2885
26. Liu JY, Iskander M (2004) Adaptive cross correlation for imaging displacements in soils. J Comput Civ Eng 18:46–57
27. Pan B, Wu DF, Wang ZY (2012) Internal displacement and strain measurement using digital volume correlation: a least-squares framework. Meas Sci Technol 23:45002
28. Mao LT, Chiang FP (2015) Interior strain analysis of a woven composite beam using X-ray computed tomography and digital volumetric speckle photography. Compos Struct 134:782–788
29. Wang E, Shukla A (2012) Blast performance of sandwich composites with in-plane compressive loading. Exp Mech 52:49–58
30. Mao LT, Chiang FP (2017) Mapping interior deformation of a composite sandwich beam using digital volumetric speckle photography with X-ray computed tomography. Compos Struct 179:172–180
31. Bergonnier S, Hild F, Roux S (2005) Digital image correlation used for mechanical tests on crimped glass wool samples. J Strain Analysis 40:185–197
32. Gates MR (2015) Subset refinement for digital volume correlation: numerical and experimental applications. Exp Mech 55:245–259
33. Limodin N, Rethore J, Adrien J, Buffiere JY, Hild F, Roux S (2011) Analysis and artifact correction for volume correlation measurements using tomographic images from a laboratory X-ray source. Exp Mech 51(6):959–970
34. Gates M, Lambros J, Heath MT (2011) Towards high performance digital volume correlation. Exp Mech 51(4):491–507